

# Nonlinear Broadband THz Generation from NV Centers in Bulk Diamond Crystals

Cormac McDonnell<sup>1\*</sup>, Hani Barhum<sup>1,2</sup>, Tamara Amro<sup>3</sup>, Pavel Ginzburg<sup>1</sup>, Nir Bar-Gill<sup>3</sup>, Aharon Blank<sup>4</sup>, Mohammad Attrash<sup>1,2</sup>

<sup>1</sup> Department of Physical Electronics, Tel Aviv University, Ramat Aviv, Tel Aviv 69978, Israel

<sup>2</sup> Triangle Research and Development Center, Kfar Qara' 3007500, Israel

<sup>3</sup> The Racah Institute of Physics, The Hebrew University of Jerusalem, Jerusalem 91904, Israel

<sup>4</sup> Schulich Faculty of Chemistry, Technion–Israel Institute of Technology, Haifa, Israel

\*cormacm@mail.tau.ac.il

Diamond single crystals could be an attractive nonlinear THz source due to the materials high damage threshold, high transparency and THz-NIR phase matching ability. However, the buildup of second order nonlinear fields is restricted due to the centrosymmetric structure of the crystal. Here, we demonstrate nonlinear broadband THz emission due to optical rectification from diamond single crystals induced by embedded symmetry breaking nitrogen vacancy (NV) centers. The nonlinear temporal and spectral emission properties of the crystal are examined using THz time domain spectroscopy after pumping with NIR femtosecond pulses. The diamond-NV cell structure was also examined using density functional theory (DFT). The results show the potential of NV centers in diamond as a new nonlinear platform for broadband efficient THz generation.

## Introduction

Negatively charged nitrogen vacancy (NV<sup>-</sup>) centers in diamond are considered an attractive platform for many applications in areas such as quantum technologies<sup>1-3</sup>. This is driven by their unique properties, such as a long spin coherence time at room temperature and a spin dependent photoluminescence. These properties have resulted in the application of NV centers to areas such as magnetic<sup>4-6</sup>, electric<sup>7</sup> and temperature sensing<sup>8-11</sup>. The NV<sup>-</sup> spin can also be manipulated through optical detection of magnetic resonance (ODMR)<sup>12</sup>. Diamond itself has been shown to be an attractive material in the field of optics due its optical and mechanical properties, including a high transparency across a large wavelength range and a high damage threshold. However nonlinear emission is limited to odd numbered nonlinear effects due to its centrosymmetric structure<sup>13,14</sup>, with second order processes in general not radiating to the far field. Various nonlinear processes have been demonstrated previously in diamond using novel schemes such as second harmonic (SH) emission due to the presence of grain boundaries<sup>15</sup>, SH emission due to an overlapping symmetry breaking THz field<sup>16</sup> and Raman-resonance enhanced four wave mixing<sup>17</sup>. Recently, NV centers in diamond irradiated with ultrashort pulses were shown to induce a dipole and quadrupole in the crystal lattice, resulting in the emission of second harmonic fields from a surface region for pump

wavelengths below the bandgap<sup>18</sup>. In the THz frequency range, NV centers in diamond were shown to emit single frequency coherent THz photons after the application of a high magnetic field<sup>19</sup>. As such, NV centers may also show promise for broadband THz generation through optical rectification of an ultrashort pump pulse. This can be coupled with the potential for NIR-THz phase matching due to the flat spectral response of diamond from the UV to THz bands. Broadband THz generation itself has been investigated in many material platforms including inorganic crystals<sup>20,21</sup>, organic crystals<sup>22,23</sup>, plasmonic metasurfaces<sup>24,25</sup> and spintronic emitters<sup>26</sup> amongst others. Here we show for the first time emission of broadband THz pulses from NV doped diamond due to optical rectification of a below bandgap NIR ultrashort pulse in the crystal. The results show a new platform with the potential for high field strength THz generation.

## Results

A 3D confocal scan of the diamond sample was done using a confocal microscope (Leica microsystems) and is shown in Fig 1a and Fig 1b. The scan shows the NV<sup>-</sup> centers distributed throughout the diamond sample (see Methods for NV fabrication details). The general crystal dimensions consist of lateral faces in the mm range, with a thickness of ~1 mm. The emission and ODMR spectrum of the sample are shown below in Figure 1 c and d respectively. The emission spectrum in Figure 1c shows a broad emission centered on approximately 675 nm. The dashed lines indicate the NV<sup>-</sup> and NV<sup>0</sup> zero phonon lines at 637 and 575 nm respectively, which agrees with previous results in the literature<sup>27</sup>. The ODMR spectrum reveals a resonance peak at 2.87 GHz, with peak splitting of 10 MHz. The peak splitting is due to strain in the crystal. The NV centers are embedded parallel to the 111 planes of the crystal.

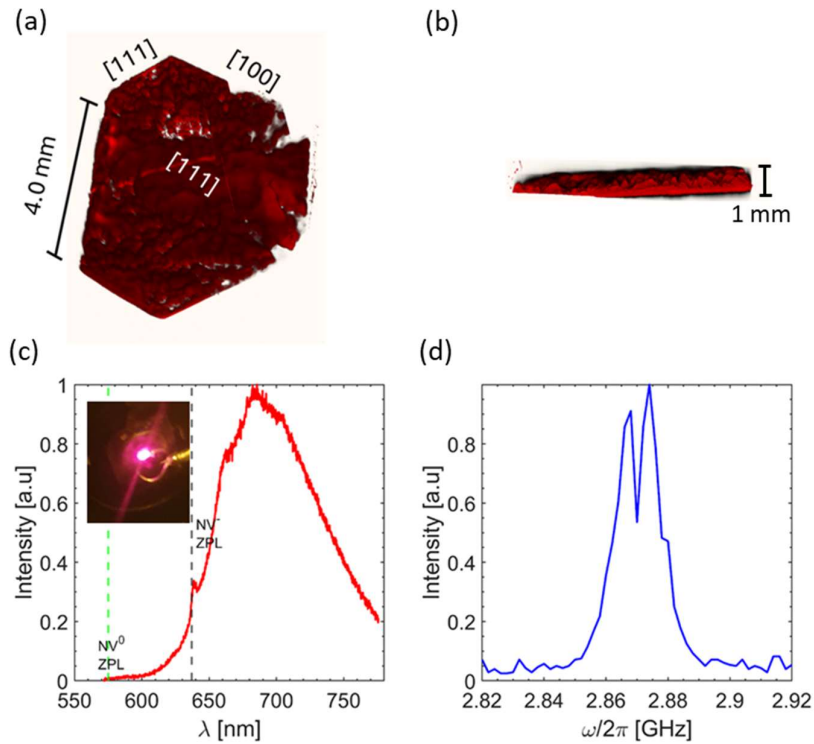


Figure 1: 3d scan of the diamond sample in confocal microscope: (a) The diamond sample with [111] face orientation and two edges of 111 and 100, the sample length is 4.0 mm. The inset shows the sample photo (b) the sample thickness is 0.1 mm. (c) Emission spectrum of the NV<sup>-</sup> crystal under excitation with a laser at a wavelength of 552 nm. Two dashed lines are positioned at the NV<sup>-</sup> and NV<sup>0</sup> zero-phonon lines (637 and 575 nm, respectively). Inset: Photo of diamond exposed to 532 nm laser (d) ODMR with no magnetic field reveals a resonance peak at 2.87 GHz. The peak splitting (10 MHz) is associated with strain.

The DFT results of NV in diamond are shown in Figure 2. Figure 2 (a) shows the diamond super cell consisting of 2 x 2 x 2 unit cells with a single NV center marked in blue. The carbon-carbon bond lengths from the simulations are 7.156 and 1.56 Å respectively. This compares well to the literature with experimental values from the literature of 7.165 and 1.55 Å. Figure 2 (b) shows the overall charge distribution in the diamond super cell, with isosurfaces equal to 1.7. Figure 2 (c) and (d) show the LUMO and HOMO orbitals.

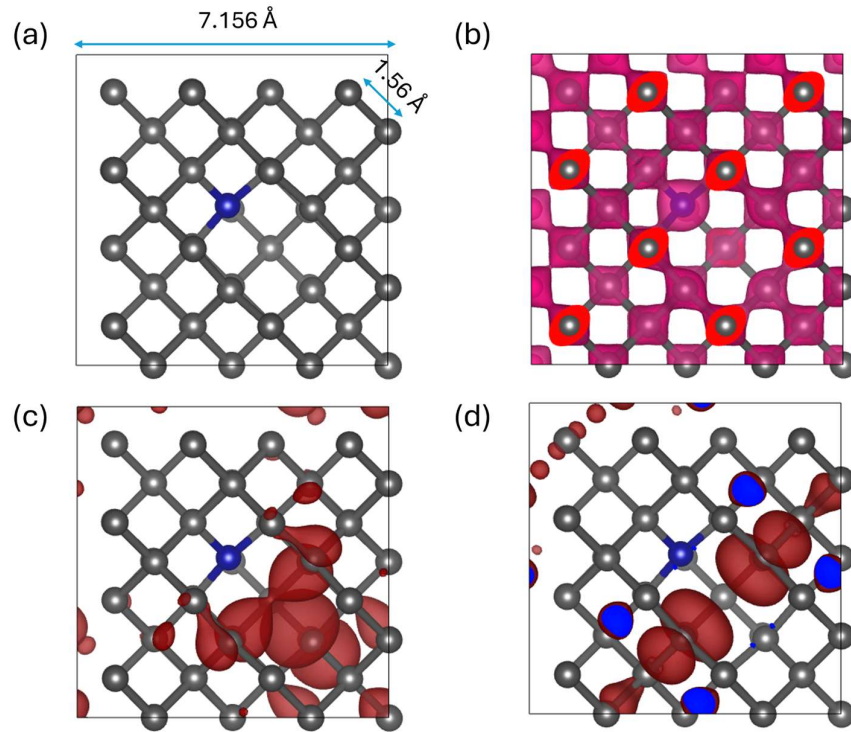


Figure 2. Optimized diamond cell according to DFT calculations. (a) A diamond super cell of  $2 \times 2 \times 2$  unit cells containing a single NV center. The carbon-carbon bond length and super cell length are 1.56 and 7.156 Å, respectively. According to experimental results, the carbon-carbon bond length and super cell length are 1.55 and 7.134 Å, respectively. (b) charge distribution in the diamond super cell, with isosurfaces equals to 1.7. (c) LUMO and (d) HOMO orbitals.

The linear and nonlinear properties of the crystal were examined in the NIR spectral range. Figure 3a shows the general orientation of the crystal, the crystal faces and the orientation axes of the pump polarization and generated THz pulse. The linear response of the crystal is shown in Fig 3b. The total transmission in the NIR range is in the region of 55 % from 900 to 1600 nm. The crystal was then pumped with NIR ultrashort pulses (1300 and 1500 nm, 50 fs, 300 GW/cm<sup>2</sup>) and the generated THz signal was examined in transmission through the crystal using a THz time domain spectroscopy setup (see Methods for a full experimental description). Figure 3 shows the time domain THz electric field traces for both wavelengths of 1300 and 1500 nm, with the linear polarization aligned to the x axis. The emitted signal shows a near single cycle waveform with a linear polarization along the y axis. Figure 3d shows the spectral information of both traces, with frequencies up to 2.5 THz measured. For both wavelengths only minor differences in the signal amplitude are observed, which is expected from the near flat transmission band in the NIR. Figure 3e shows the measured THz field intensity as a function of the pump intensity. The THz intensity increases with a second order trend with respect to the pump intensity, as expected for such a nonlinear process. No saturation of the generated THz intensity was observed for the range of pump intensities used. Also, the effect of the pump linear polarization angle on the THz field strength was examined, shown in Figure 3f. In general, THz emission is observed along the y polarization direction for all input pump polarization angles, with some minor deviations in the overall field strength depending on the pump angle. This general lack of a preferred illumination axis is expected from the general

nature of the random embedded NV centers throughout the sample. Finally, the THz electric field strength was compared to a standard ZnTe crystal ( $d = 100 \mu\text{m}$ ), for both crystals at a wavelength of 1500 nm and a pump intensity of 300  $\text{GW}/\text{cm}^2$ . The resulting peak THz electric field emitted from the ZnTe was approximately 15 times more than the diamond NV sample. This lower emission compared to ZnTe may be due to a number of crystal properties which may lead to a non-ideal environment for optical rectification of the pumping pulse. Firstly, the density of NV's and the fabrication method leads to a transmission through the crystal of approximately 55 % in the NIR. Potentially reducing the NV density may result in higher pump transmission and also lower reabsorption of the generated THz pulse. In the current configuration, it is likely that only emission from the end section of the crystal is contributing to the buildup of the THz pulse. Further investigations into the NV fabrication method and conditions may lead to better pump-THz phase matching, resulting in increased THz field emission.

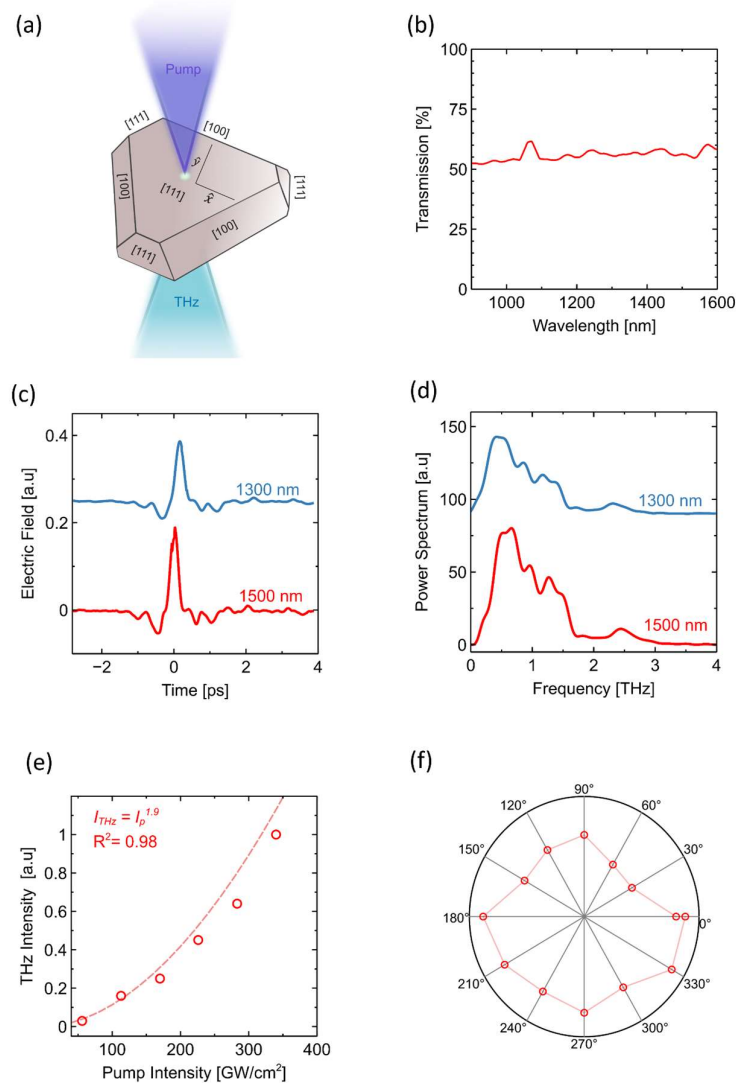


Figure 3 (a) Schematic of the diamond crystal showing the relative orientations of the crystal face, direction of pump incidence and the THz transmission direction. The pump polarization was rotated in the x-y plane (b) Linear transmission of the diamond crystal in the NIR range, with typical values around 55 %. The peak at 1064 nm is due to the supercontinuum light source. (c) Time domain electric field traces for two pump wavelengths of 1500

and 1300 nm at input intensities of 300 GW/cm<sup>2</sup>. The two datasets are offset for clarity. (d) Spectral information from the corresponding time traces, showing THz frequencies up to 2.5 THz. (e) THz electric field as a function of the incident pump intensity. The fit goes to the power of 1.9. (f) Peak THz field as a function of the linear input polarization angle, where 0° and 90° correspond to the x and y axes.

## Conclusions

Here we show for the first time emission of broadband THz pulses from NV centers in diamond due to optical rectification of an ultrashort pump pulse. The embedded NV centers induce a dipole in the normally symmetric crystal allowing the emission of second order nonlinear fields. Further investigations into the NV implantation and fabrication methods are needed to find the optimum crystal conditions which will result in NIR-THz phase matching, which will result in a greatly increased THz field emission efficiency.

## Methods

### Experimental

An HPHT diamond 111 sample type Ib (element 6) with a nitrogen concentration lower than 200 ppm was used. NV<sup>-</sup> was activated by exposing the sample with e<sup>-</sup> irradiation at an energy of 5 MeV with a dose of 10<sup>9</sup> cm<sup>-2</sup> and annealing at 700 °C for 90 hours. The NV<sup>-</sup> concentration is estimated to be 20 ppm distributed throughout the crystal.

The THz emission properties of the crystal were characterized using a THz time domain spectroscopy setup. The crystal was pumped using the output of the optical parametric amplifier (OPA) system with a tunable wavelength in the NIR with a pulse duration of approximately 50 fs. The OPA system was pumped using a Ti:Sa laser at 800 nm, for which a 1 % portion was split for the probe line of the time domain system. The output of the OPA was sent to the pump line, where a number of optical elements were used to control the beam size, power and polarization. The generated THz signal was collimated using an off-axis parabolic mirror (f = 50 mm). The THz was then focussed into a ZnTe nonlinear detection crystal (d = 500 μm) where it was temporally and spatially overlapped with the probe pulse. The amplitude and phase of the generated THz pulse was recorded using an electro-optic detection scheme, consisting of a quarter waveplate, Wollaston prism and a balanced photodetector. The signal was averaged over 300 ms using a lock-in amplifier.

### Theoretical

DFT was used to investigate the diamond NV cell structure. A cell consisted of 62 carbon atoms and the effect of a single NV was investigated<sup>28</sup>. The calculations were performed by the plane-wave Quantum Espresso package<sup>29</sup> and Perdew-Burke-Ernzerhof (PBE)<sup>30</sup> exch-corr scalar relativistic ultrasoft pseudopotential. Vdw-df-cx non-local density functional for van der Waals interactions was used<sup>31-34</sup>. A supercell of the size 2×2×2 was used and the Vesta<sup>35</sup> program was used for structure plotting.

## Appendix

The dielectric constants in cartesian axis according to the DFT calculations are:

$$\begin{pmatrix} 6.620516625 & 0.315725509 & 0.315725509 \\ 0.315725274 & 6.621599917 & -0.280794958 \\ 0.315725274 & -0.280794958 & 6.621599917 \end{pmatrix}$$

## References

- (1) Kim, D.; Ibrahim, M. I.; Foy, C.; Trusheim, M. E.; Han, R.; Englund, D. R. A CMOS-Integrated Quantum Sensor Based on Nitrogen–Vacancy Centres. *Nat Electron* **2019**, *2* (7), 284–289. <https://doi.org/10.1038/s41928-019-0275-5>.
- (2) Nizovtsev, A. P.; Kilin, S. Ya.; Jelezko, F.; Gaebel, T.; Popa, I.; Gruber, A.; Wrachtrup, J. A Quantum Computer Based on NV Centers in Diamond: Optically Detected Nutations of Single Electron and Nuclear Spins. *Opt. Spectrosc.* **2005**, *99* (2), 233–244. <https://doi.org/10.1134/1.2034610>.
- (3) Chakraborty, T.; Lehmann, F.; Zhang, J.; Borgsdorf, S.; Wöhrle, N.; Remfort, R.; Buck, V.; Köhler, U.; Suter, D. CVD Growth of Ultrapure Diamond, Generation of NV Centers by Ion Implantation, and Their Spectroscopic Characterization for Quantum Technological Applications. *Phys. Rev. Mater.* **2019**, *3* (6), 065205. <https://doi.org/10.1103/PhysRevMaterials.3.065205>.
- (4) Maze, J. R.; Stanwix, P. L.; Hodges, J. S.; Hong, S.; Taylor, J. M.; Cappellaro, P.; Jiang, L.; Dutt, M. V. G.; Togan, E.; Zibrov, A. S.; Yacoby, A.; Walsworth, R. L.; Lukin, M. D. Nanoscale Magnetic Sensing with an Individual Electronic Spin in Diamond. *Nature* **2008**, *455* (7213), 644–647. <https://doi.org/10.1038/nature07279>.
- (5) Wolf, T.; Neumann, P.; Nakamura, K.; Sumiya, H.; Ohshima, T.; Isoya, J.; Wrachtrup, J. Subpicotesla Diamond Magnetometry. *Phys. Rev. X* **2015**, *5* (4), 041001. <https://doi.org/10.1103/PhysRevX.5.041001>.
- (6) Taylor, J. M.; Cappellaro, P.; Childress, L.; Jiang, L.; Budker, D.; Hemmer, P. R.; Yacoby, A.; Walsworth, R.; Lukin, M. D. High-Sensitivity Diamond Magnetometer with Nanoscale Resolution. *Nature Phys* **2008**, *4* (10), 810–816. <https://doi.org/10.1038/nphys1075>.
- (7) Dolde, F.; Fedder, H.; Doherty, M. W.; Nöbauer, T.; Rempp, F.; Balasubramanian, G.; Wolf, T.; Reinhard, F.; Hollenberg, L. C. L.; Jelezko, F.; Wrachtrup, J. Electric-Field Sensing Using Single Diamond Spins. *Nature Phys* **2011**, *7* (6), 459–463. <https://doi.org/10.1038/nphys1969>.
- (8) Toyli, D. M.; Christle, D. J.; Alkauskas, A.; Buckley, B. B.; Van de Walle, C. G.; Awschalom, D. D. Measurement and Control of Single Nitrogen-Vacancy Center Spins above 600 K. *Phys. Rev. X* **2012**, *2* (3), 031001. <https://doi.org/10.1103/PhysRevX.2.031001>.
- (9) Acosta, V. M.; Bauch, E.; Ledbetter, M. P.; Waxman, A.; Bouchard, L.-S.; Budker, D. Temperature Dependence of the Nitrogen-Vacancy Magnetic Resonance in Diamond. *Phys. Rev. Lett.* **2010**, *104* (7), 070801. <https://doi.org/10.1103/PhysRevLett.104.070801>.
- (10) Doherty, M. W.; Acosta, V. M.; Jarmola, A.; Barson, M. S. J.; Manson, N. B.; Budker, D.; Hollenberg, L. C. L. Temperature Shifts of the Resonances of the  $\{\mathrm{NV}\}^{\{\ensurerm{-}\}}$  Center in Diamond. *Phys. Rev. B* **2014**, *90* (4), 041201. <https://doi.org/10.1103/PhysRevB.90.041201>.
- (11) Attrash, M.; Shtempluck, O.; Buks, E. High Temperature Spectroscopy of Ensembles of Nitrogen-Vacancy Centers in Diamond. *Journal of Applied Physics* **2023**, *133* (9).
- (12) Gruber, A.; Dräbenstedt, A.; Tietz, C.; Fleury, L.; Wrachtrup, J.; Borczykowski, C. von. Scanning Confocal Optical Microscopy and Magnetic Resonance on Single Defect Centers. *Science* **1997**, *276* (5321), 2012–2014. <https://doi.org/10.1126/science.276.5321.2012>.
- (13) Abulikemu, A.; Hase, M. Highly-Efficient Third-Harmonic Generation from Ultrapure Diamond Crystals. *Opt. Mater. Express, OME* **2023**, *13* (4), 916–924. <https://doi.org/10.1364/OME.485601>.
- (14) Apostolova, T.; Obreshkov, B. High Harmonic Generation from Bulk Diamond Driven by Intense Femtosecond Laser Pulse. *Diamond and Related Materials* **2018**, *82*, 165–172. <https://doi.org/10.1016/j.diamond.2017.12.013>.
- (15) Trojánek, F.; Židek, K.; Dzurňák, B.; Kozák, M.; Malý, P. Nonlinear Optical Properties of Nanocrystalline Diamond. *Opt. Express* **2010**, *18* (2), 1349. <https://doi.org/10.1364/OE.18.001349>.
- (16) Petev, M.; NiclasWesterberg; Rubino, E.; Moss, D.; Couairon, A.; Légaré, F.; Morandotti, R.; Faccio, D.; Clerici, M. Phase-Insensitive Scattering of Terahertz Radiation. *Photonics* **2017**, *4* (1), 7. <https://doi.org/10.3390/photonics4010007>.

- (17) Le, J.; Su, Y.; Tian, C.; Kung, A. H.; Shen, Y. R. A Novel Scheme for Ultrashort Terahertz Pulse Generation over a Gapless Wide Spectral Range: Raman-Resonance-Enhanced Four-Wave Mixing. *Light Sci Appl* **2023**, *12* (1), 34. <https://doi.org/10.1038/s41377-023-01071-z>.
- (18) Abulikemu, A.; Kainuma, Y.; An, T.; Hase, M. Second-Harmonic Generation in Bulk Diamond Based on Inversion Symmetry Breaking by Color Centers. *ACS Photonics* **2021**, *8* (4), 988–993. <https://doi.org/10.1021/acsp Photonics.0c01806>.
- (19) Kollarics, S.; Márkus, B. G.; Kucsera, R.; Thiering, G.; Gali, Á.; Németh, G.; Kamarás, K.; Forró, L.; Simon, F. Terahertz Emission from Diamond Nitrogen-Vacancy Centers. *Science Advances* **2024**, *10* (22), eadn0616. <https://doi.org/10.1126/sciadv.adn0616>.
- (20) Carletti, L.; McDonnell, C.; Arregui Leon, U.; Rocco, D.; Finazzi, M.; Toma, A.; Ellenbogen, T.; Della Valle, G.; Celebrano, M.; De Angelis, C. Nonlinear THz Generation through Optical Rectification Enhanced by Phonon–Polaritons in Lithium Niobate Thin Films. *ACS Photonics* **2023**, *10* (9), 3419–3425. <https://doi.org/10.1021/acsp Photonics.3c00924>.
- (21) Hu, L.; Wang, B.; Guo, Y.; Du, S.; Chen, J.; Li, J.; Gu, C.; Wang, L. Quasi-BIC Enhanced Broadband Terahertz Generation in All-Dielectric Metasurface. *Advanced Optical Materials* **2022**, *10* (12), 2200193. <https://doi.org/10.1002/adom.202200193>.
- (22) Barhum, H.; McDonnell, C.; Alon, T.; Hammad, R.; Attrash, M.; Ellenbogen, T.; Ginzburg, P. Organic Kainate Single Crystals for Second-Harmonic and Broadband THz Generation. *ACS Appl. Mater. Interfaces* **2023**, *15* (6), 8590–8600. <https://doi.org/10.1021/acsam.2c18454>.
- (23) Vicario, C.; Jazbinsek, M.; Ovchinnikov, A. V.; Chefonov, O. V.; Ashitkov, S. I.; Agranat, M. B.; Hauri, C. P. High Efficiency THz Generation in DSTMS, DAST and OH1 Pumped by Cr:Forsterite Laser. *Opt. Express, OE* **2015**, *23* (4), 4573–4580. <https://doi.org/10.1364/OE.23.004573>.
- (24) Sideris, S.; Zixian, H.; McDonnell, C.; Li, G.; Ellenbogen, T. Holographic THz Beam Generation by Nonlinear Plasmonic Metasurface Emitters. *ACS Photonics* **2023**, *10* (8), 2972–2979. <https://doi.org/10.1021/acsp Photonics.3c00775>.
- (25) McDonnell, C.; Deng, J.; Sideris, S.; Ellenbogen, T.; Li, G. Functional THz Emitters Based on Pancharatnam-Berry Phase Nonlinear Metasurfaces. *Nat Commun* **2021**, *12* (1), 30. <https://doi.org/10.1038/s41467-020-20283-0>.
- (26) Agarwal, P.; Mishra, S. S.; Medwal, R.; Mohan, J. R.; Asada, H.; Fukuma, Y.; Singh, R. Reconfigurable Chiral Spintronic THz Emitters. *Advanced Optical Materials* **2024**, *12* (20), 2303128. <https://doi.org/10.1002/adom.202303128>.
- (27) Manson, N. B.; Beha, K.; Batalov, A.; Rogers, L. J.; Doherty, M. W.; Bratschitsch, R.; Leitenstorfer, A. Assignment of the NV<sup>0</sup> 575-Nm Zero-Phonon Line in Diamond to a  $E_{2A_2}$  Transition. *Phys. Rev. B* **2013**, *87* (15), 155209. <https://doi.org/10.1103/PhysRevB.87.155209>.
- (28) Kohn, W.; Sham, L. J. Self-Consistent Equations Including Exchange and Correlation Effects. *Phys. Rev.* **1965**, *140* (4A), A1133–A1138. <https://doi.org/10.1103/PhysRev.140.A1133>.
- (29) Giannozzi, P.; Baroni, S.; Bonini, N.; Calandra, M.; Car, R.; Cavazzoni, C.; Ceresoli, D.; Chiarotti, G. L.; Cococcioni, M.; Dabo, I.; Corso, A. D.; Gironcoli, S. de; Fabris, S.; Fratesi, G.; Gebauer, R.; Gerstmann, U.; Gougoussis, C.; Kokalj, A.; Lazzeri, M.; Martin-Samos, L.; Marzari, N.; Mauri, F.; Mazzarello, R.; Paolini, S.; Pasquarello, A.; Paulatto, L.; Sbraccia, C.; Scandolo, S.; Sclauzero, G.; Seitsonen, A. P.; Smogunov, A.; Umari, P.; Wentzcovitch, R. M. QUANTUM ESPRESSO: A Modular and Open-Source Software Project for Quantum Simulations of Materials. *J. Phys.: Condens. Matter* **2009**, *21* (39), 395502. <https://doi.org/10.1088/0953-8984/21/39/395502>.
- (30) Perdew, J. P.; Burke, K.; Ernzerhof, M. Generalized Gradient Approximation Made Simple (Vol 77, Pg 3865, 1996). *Physical Review Letters* **1997**, *78* (7), 1396–1396.
- (31) Thonhauser, T.; Zuluaga, S.; Arter, C. A.; Berland, K.; Schröder, E.; Hyldgaard, P. Spin Signature of Nonlocal Correlation Binding in Metal-Organic Frameworks. *Phys. Rev. Lett.* **2015**, *115* (13), 136402. <https://doi.org/10.1103/PhysRevLett.115.136402>.
- (32) Thonhauser, T.; Cooper, V. R.; Li, S.; Puzder, A.; Hyldgaard, P.; Langreth, D. C. Van Der Waals Density Functional: Self-Consistent Potential and the Nature of the van Der Waals Bond. *Phys. Rev. B* **2007**, *76* (12), 125112. <https://doi.org/10.1103/PhysRevB.76.125112>.
- (33) Berland, K.; Cooper, V. R.; Lee, K.; Schröder, E.; Thonhauser, T.; Hyldgaard, P.; Lundqvist, B. I. Van Der Waals Forces in Density Functional Theory: A Review of the vdW-DF Method. *Reports on Progress in Physics* **2015**, *78* (6), 066501.
- (34) Langreth, D. C.; Lundqvist, B. I.; Chakarova-Käck, S. D.; Cooper, V. R.; Dion, M.; Hyldgaard, P.; Kelkkänen, A.; Kleis, J.; Kong, L.; Li, S. A Density Functional for Sparse Matter. *Journal of Physics: Condensed Matter* **2009**, *21* (8), 084203.
- (35) Momma, K.; Izumi, F. VESTA 3 for Three-Dimensional Visualization of Crystal, Volumetric and Morphology Data. *Journal of Applied Crystallography* **2011**, *44* (6), 1272–1276. <https://doi.org/10.1107/S0021889811038970>.